

# Universal Fabrication of 2D Electron Systems in Functional Oxides

Tobias Chris Rödel, Franck Fortuna, Shamashis Sengupta, Emmanouil Frantzeskakis, Patrick Le Fèvre, François Bertran, Bernard Mercey, Sylvia Matzen, Guillaume Agnus, Thomas Maroutian, Philippe Lecoeur, and Andrés Felipe Santander-Syro\*

A critical challenge of modern materials science is to tailor novel states of matter suitable for future applications beyond semiconductor technology. 2D electron systems (2DESs) in multi-functional oxides<sup>[1]</sup> can show metal-to-insulator transitions,<sup>[2]</sup> superconductivity,<sup>[3,4]</sup> magnetism,<sup>[5–7]</sup> or spin-polarized states,<sup>[8–10]</sup> and are thus an active field of current research.<sup>[11–13]</sup>

However, the fabrication of 2DESs in oxide heterostructures, like  $\text{LaAlO}_3/\text{SrTiO}_3$ , requires growing a layer of binary (e.g.,  $\text{Al}_2\text{O}_3$ ) or ternary (e.g.,  $\text{LaAlO}_3$ ) oxides with a “critical thickness” of at least 20 Å using evolved deposition techniques, such as pulsed laser deposition.<sup>[1,11–17]</sup> Thus, the reproducibility of their properties depends crucially on the growth parameters, while their fabrication is complex, expensive, and unsuitable for mass production. Moreover, the existence of a critical thickness of 20 Å for the onset of conductivity severely limits the control of the 2DESs properties, hampering tunneling spectroscopy studies or applications that rely on charge or spin injection.<sup>[18]</sup> Similarly, the realization of 2DESs at the surface of  $\text{SrTiO}_3$  or other oxides requires the use of intense UV or X-ray synchrotron radiation, to desorb oxygen from the surface.<sup>[19–26]</sup> Thus,

these 2DESs can be only manipulated and studied in ultra-high vacuum (UHV), to preserve the vacancies from re-oxidation, and are obviously not suited for experiments or applications at ambient conditions.

Here we demonstrate a new, wholly general, extremely simple and cost-effective method to generate 2DESs in functional oxides. We use thermal evaporation from a Knudsen cell to deposit, at room temperature in UHV, an atomically-thin layer of an elementary reducing agent, such as pure aluminum, on the oxide surface. Due to an efficient redox reaction, the Al film pumps oxygen from the substrate, oxidizes into insulating  $\text{AlO}_x$ , and forms a pristine, homogeneous 2DES in the first atomic planes of the underlying oxide. The principle of redox reactions induced by metals at the surface of oxides is well documented.<sup>[27,28]</sup> However, the simple idea of using a pure, elementary reducing agent to create a 2DES at a metal–oxide interface was not explored so far. This overcomes the complexity of growing an oxide thin film, the requirement of a critical thickness of insulating capping layer to create the 2DES in UHV, and the necessity, in the case of surfaces, of strong synchrotron radiation to desorb oxygen. As a novel application, we extend this method to generate a 2D metallic state at the surface of the room-temperature ferroelectric  $\text{BaTiO}_3$ . Such hitherto unobserved coexistence of ferroelectricity and 2D conductivity in the same material is promising for functional devices using ferroelectric resistive switching.<sup>[29,30]</sup> This new, simpler and cheaper, fabrication route for 2DESs is thus adaptable to numerous oxides, given that oxygen vacancies are shallow donors in these materials, resulting in itinerant electrons. Moreover, this technique is scalable to industrial production, and ideally suited for applications that rely on charge or spin injection and for the realization of mesoscopic devices.

The existence of a 2DES at the interface between the oxidized Al layer and  $\text{SrTiO}_3(001)$ ,  $\text{SrTiO}_3(111)$  and anatase- $\text{TiO}_2(001)$  is evidenced by our angle-resolved photoemission spectroscopy (ARPES) data presented in Figure 1—see the Supporting Information for details about the surface preparation, Al deposition, and ARPES measurements. For simplicity, and to recall that we are simply depositing pure Al (not aluminum oxide) on top of the oxide surfaces, all throughout this paper we note the resulting oxidized Al capping layer simply as “Al,” specifying in parenthesis the evaporated thickness. The energy-momentum and Fermi surface maps formed by the  $t_{2g}$  orbitals, shown in Figure 1, agree with previous ARPES studies at the reduced surface of these materials,<sup>[19,20,24–26,31]</sup> demonstrating that in both cases the same 2DESs are observed.

T. C. Rödel, Dr. F. Fortuna, Dr. E. Frantzeskakis,  
Dr. A. F. Santander-Syro  
CSNSM, Univ. Paris-Sud  
CNRS/IN2P3  
Université Paris-Saclay  
91405 Orsay, France  
E-mail: andres.santander@csnsm.in2p3.fr

T. C. Rödel, Dr. P. Le Fèvre, Dr. F. Bertran  
Synchrotron SOLEIL  
L'Orme des Merisiers  
Saint-Aubin-BP48  
91192 Gif-sur-Yvette, France

Dr. S. Sengupta  
Laboratoire de Physique des Solides  
Univ. Paris-Sud, CNRS  
Université Paris-Saclay  
91405 Orsay, France

Prof. B. Mercey  
CRISMAT, ENSICAEN-CNRS UMR6508  
6 bd. Maréchal Juin  
14050 Caen, France

Dr. S. Matzen, Dr. G. Agnus, Dr. T. Maroutian, Prof. P. Lecoeur  
Institut d'Electronique Fondamentale  
Univ. Paris-Sud  
CNRS, Université Paris-Saclay  
91405 Orsay, France



DOI: 10.1002/adma.201505021

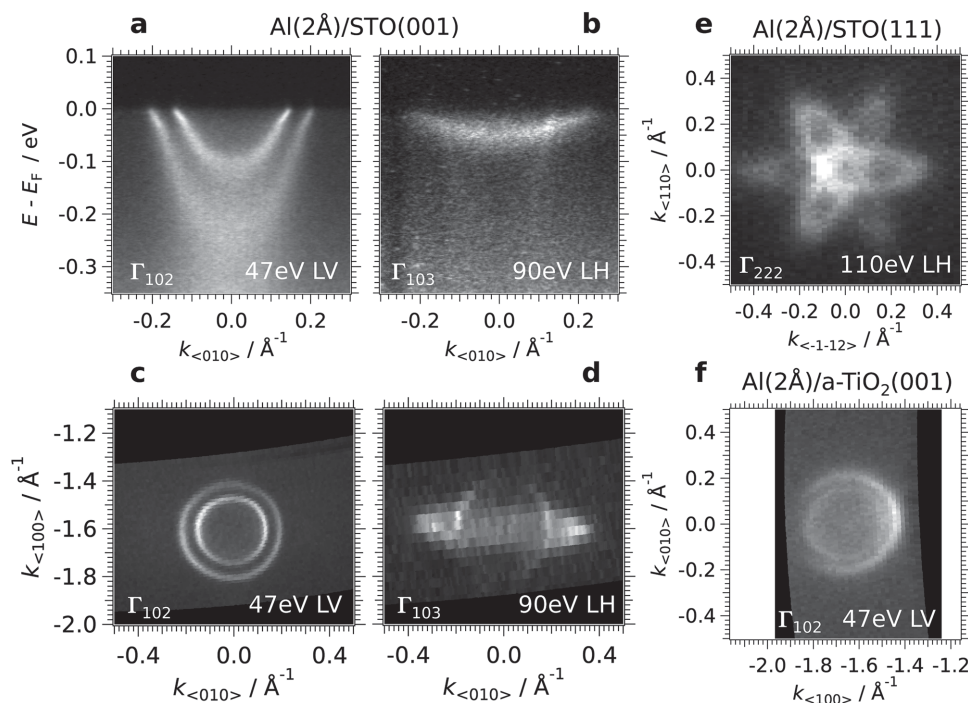


**Figure 1.** **a,b)** ARPES energy-momentum intensity maps measured at the Al(2 Å)/SrTiO<sub>3</sub>(001) interface prepared in situ, using respectively 47 eV linear vertical (LV) and 90 eV linear horizontal (LH) photons. **c,d)** Corresponding Fermi surface maps. Data at  $h\nu = 47$  eV were measured around the  $\Gamma_{102}$  point, while data at  $h\nu = 90$  eV were measured around  $\Gamma_{103}$ . **e,f)** Fermi surface maps measured at the Al/SrTiO<sub>3</sub>(111) and Al/TiO<sub>2</sub>(001) anatase interfaces prepared in situ. Unless specified otherwise, all spectra in this and remaining figures were measured at  $T = 8$  K.

Note that, instead of the local creation of oxygen vacancies using an intense UV beam, the evaporated Al reduces the whole surface homogeneously. As a consequence, the data quality, evidenced by the line widths, is also much better than in previous studies. Thus, as shown in Figure 1a, a kink and change in intensity in the dispersion of the light bands at  $E \approx -30$  meV, attributed to electron-phonon coupling,<sup>[32]</sup> can be very clearly distinguished.

The Fermi-surface areas and, hence, the charge carrier densities of the 2DESs at the Al/SrTiO<sub>3</sub>(111) and Al/TiO<sub>2</sub>(001) interfaces are about 1.3 and 2 times larger than their counterparts at the surfaces reduced by photons, probably due to a higher and more homogeneous concentration of oxygen vacancies.

To understand the redox reaction at the Al/oxide interface, we probed the oxidation state of Al by measuring the Al-2*p* core levels, whose binding energies are very different for metallic and oxidized Al. As shown in Figure 2a, the two contributions can be distinguished in the Al(6 Å)/STO spectrum (blue curve), with the metallic component around 72.5 eV binding energy and the oxidized part around 75 eV binding energy. In contrast, the metallic Al component decreases for a thinner 4 Å film (black curve), and the deposition of only 2 Å of pure Al results in a nearly fully oxidized film of Al (red curves). In other words, an ultra-thin layer of 2 Å of pure Al is sufficient to pump the oxygen from the surface region of all the oxides studied in this work. The spatial distribution of the oxygen vacancies close to the interface is discussed in the Supporting Information. Note that the oxidation of the metallic Al results in an increased layer thickness: as the mass density of Al is 2.7 g cm<sup>-3</sup> and the one of amorphous Al<sub>2</sub>O<sub>3</sub> is about 4 g cm<sup>-3</sup>, the deposition of 2 Å of Al yields an oxidized Al film of 2.5 Å.

To determine if the thickness of the Al-layer has an influence on the electron density of the 2DES, we turn to the momentum distribution curves (MDCs) at the Fermi level as shown in Figure 2b. As can be seen in Figure 2b, the Fermi momenta are essentially the same, within 0.01 Å<sup>-1</sup> for the 2 Å (red MDC), 4 Å (black) and 6 Å (blue) thick Al films. As the 2D density of electrons depends solely on the Fermi momenta, it is clear that this electron density already saturates at an Al film thickness of 2 Å. Thus, our method overcomes the necessity of a “critical thickness” of capping layer to generate a 2DES in UHV.

Previous studies on the bare surface of SrTiO<sub>3</sub> prepared in situ showed that synchrotron UV-irradiation was necessary to create the oxygen vacancies responsible for the 2DES.<sup>[20,25,26,31]</sup> This is again demonstrated in the lower panel of Figure 2c, which shows the evolution with time of the MDC at  $E_F$  upon UV-irradiation on a bare SrTiO<sub>3</sub>(001) surface. While the 2DES is absent at  $t = 0$  h (black MDC), its carrier density increases up to saturation upon UV irradiation (blue and red MDCs), as denoted by the increase of  $k_F$  for increasing exposure times.

Contrary to the bare surface, there is no measurable influence of the UV irradiation on the electronic structure of the Al/SrTiO<sub>3</sub> system, neither on the charge carrier density nor on the line-shapes or spectral weight of the 2DES, as demonstrated in the top panel of Figure 2c: the MDCs at  $E_F$  show a stable sub-band structure and a maximum electron density from the very beginning of the measurements. This indicates that the oxygen vacancy concentration and distribution, due the redox reaction at the interface between Al and SrTiO<sub>3</sub>, is already saturated and stable upon irradiation.

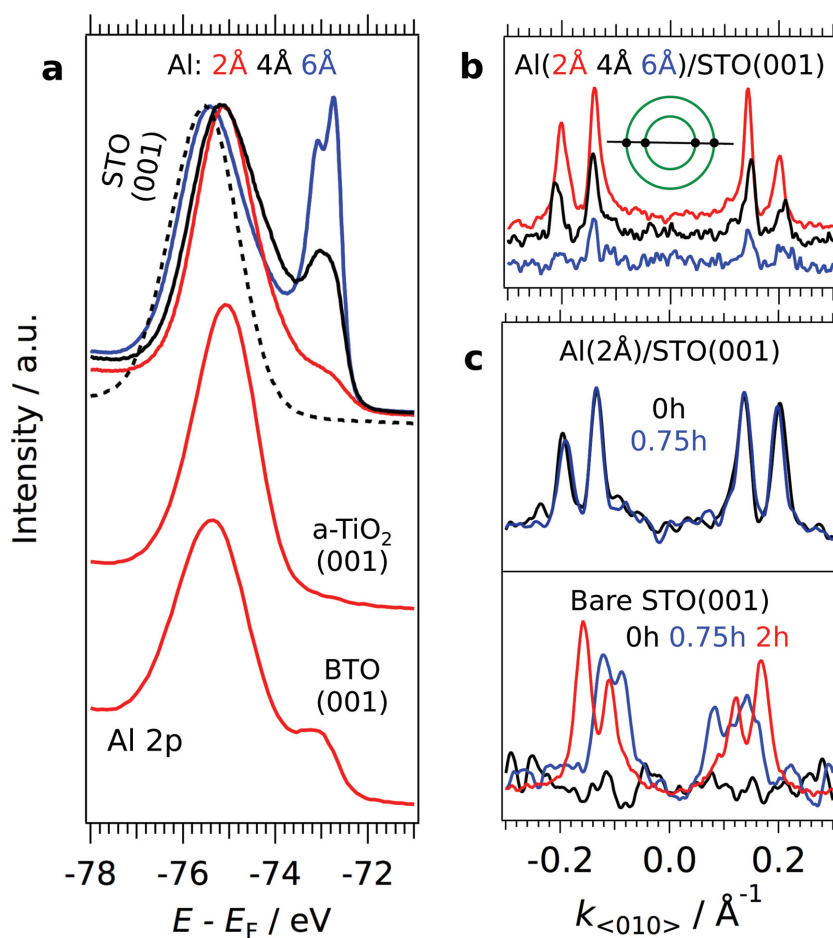


**Figure 2.** a) Angle-integrated spectra of the Al 2p peak of the Al/SrTiO<sub>3</sub>(001), Al/TiO<sub>2</sub> anatase and Al/BaTiO<sub>3</sub>(001) interfaces measured at a photon energy of  $h\nu = 100$  eV. The curves in different colors correspond to different thicknesses of Al (red 2 Å, black 4 Å, blue 6 Å). The peak shape of the Al 2p peak indicates if the Al layer is oxidized or metallic. The dashed black curve corresponds to a fully oxidized Al layer, obtained after annealing the sample with 4 Å Al capping at 250 °C in UHV. b) Momentum distribution curves (MDCs) at  $E_F$ , along the Fermi-surface cut schematized in the inset, measured at the Al/SrTiO<sub>3</sub>(001) interface at  $h\nu = 47$  eV for different Al thicknesses. Peaks in the MDCs correspond to the Fermi momenta, where the MDC cuts the Fermi surface. The decrease in intensity of the MDCs for increasing Al thickness is merely due to increased damping of the photoemission signal. c) MDCs integrated over  $E_F \pm 5$  meV for increasing UV exposure times on the Al/SrTiO<sub>3</sub>(001) interface and the bare STO surface measured under identical conditions. The similarity of the two MDCs at the interface is in strong contrast to the evolution under light irradiation of the MDCs at the bare surface.

As demonstrated in the Supporting Information, the 2DES at the interface of oxidized Al/SrTiO<sub>3</sub> is stable also at room temperature, while the deposition of an Al film of 10 Å or more on SrTiO<sub>3</sub> minimizes the re-oxidation of vacancies in air.

We now show that the deposition of an ultrathin Al film can also be used to create a 2DES at the surface of the room-temperature ferroelectric BaTiO<sub>3</sub> (BTO), thus constituting a new type of confined metallic state on a truly room-temperature functional oxide. Our BTO samples are (001)-oriented thin films (thickness 30 nm) epitaxially grown on SrTiO<sub>3</sub>(001)—see Supporting Information for details about thin-film growth, piezo-response force microscopy (PFM), and capacitance–voltage (C–V) measurements. In contrast to the bulk crystals, which usually exhibit ferroelectric-domain stripes of period  $\approx 50$ –200 nm, even down

to 100 nm scale thicknesses,<sup>[33]</sup> the 30 nm-thick BTO films deposited on Nb:STO show a single domain state, with the ferroelectric polarization aligned along the [001] axis, due to the in-plane compressive strain induced by the epitaxial growth.<sup>[34–36]</sup>

The absence of ferroelectric domains and the local reversibility of the polarization are demonstrated in Figure 3a,b by the simultaneous atomic force microscopy (AFM) and PFM images of a BaTiO<sub>3</sub>/Nb:SrTiO<sub>3</sub> thin film.

The energy-momentum ARPES intensity maps of Figure 3c,d,e prove the formation of metallic itinerant states at the surface of the BTO(001) thin-film after deposition of 2 Å of Al. The resulting 2DES is constituted of a light ( $d_{xy}$ -like) and a heavy ( $d_{xz}/yz$ -like) electron pocket around  $\Gamma$ , best observed in Figure 3c,d with LV and LH polarizations, respectively. Such light-polarization-dependent selection rules are typical for  $t_{2g}$ -like states observed at the surface of other titanates, such as SrTiO<sub>3</sub> and anatase.<sup>[19,26]</sup> In the case of BaTiO<sub>3</sub>, the light band forms a strong peak of spectral weight whose intensity is cut-off at  $E_F$ —see Figure 3c. Although we cannot observe a dispersive feature within this peak of intensity, its binding energy indicates that the conduction band bottom is filled up with itinerant electrons. The heavy band, on the other hand, presents a clear dispersion—see Figure 3d,e. A tight-binding fit of this band, red curve in Figure 3e, yields a band bottom of  $-115$  meV at  $\Gamma$ , a band top of  $-35$  meV at the zone edge, and an effective mass near  $\Gamma$  of approximately  $12m_e$ .

Figure 3f,g show that the spectral weight at  $E_F$  is composed of a central disc formed by the light electron pocket, best seen in Figure 3g, and two orthogonal Fermi surface strips spanning the entire Brillouin zone, formed by the heavy bands. These heavy bands correspond to the elliptical Fermi sheets observed at the surface of SrTiO<sub>3</sub>(001), as in Figure 1d, but in the case of BaTiO<sub>3</sub>(001) they extend beyond the zone boundary, thus forming open Fermi sheets. From Figure 3g, the distribution of spectral weight at  $E_F$  for the circular Fermi surface spans a Fermi momentum  $k_F \approx 0.15 \pm 0.02$  Å<sup>-1</sup>. The Fermi strips can be approximated as rectangles of long and short sides  $k_l = 2 \times \pi/a$  (with  $a = 4$  Å the size of the square unit cell at the BTO surface) and  $k_s = 0.15 \pm 0.02$  Å<sup>-1</sup>. From the total area  $A_F$  enclosed by all the Fermi surfaces, the density of carriers of the 2DES at the BaTiO<sub>3</sub>(001) surface is  $n_{2D} = A_F/(2\pi^2) \approx (2.8 \pm 0.4) \times 10^{14}$  cm<sup>-2</sup>, which is comparable to the density of states at the SrTiO<sub>3</sub> or anatase-TiO<sub>2</sub> surfaces. The Supporting Information presents additional data showing the Fermi momenta extracted from fits to the spectra, and the photon-energy dependence of the electronic structure.



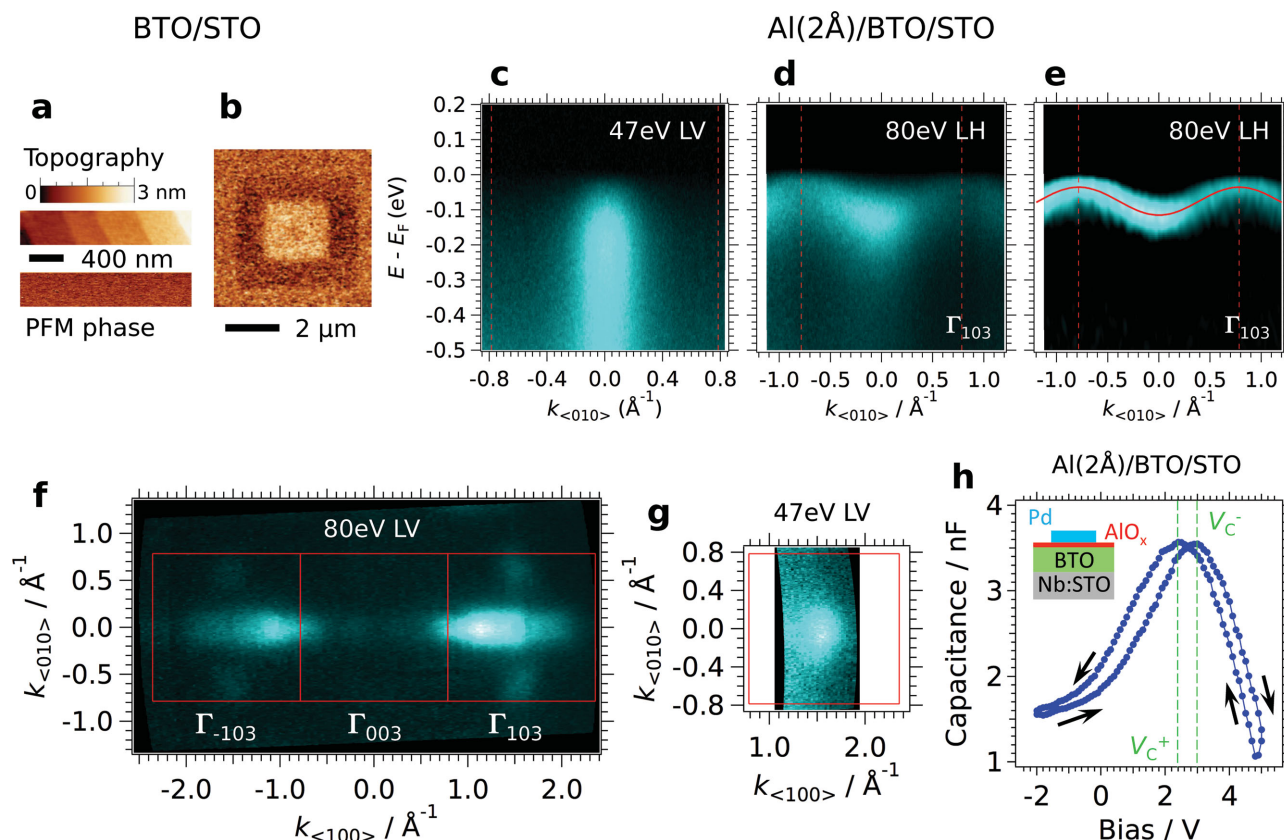


**Figure 3.** a) AFM topography and corresponding PFM phase signal measured on a 30 nm thick BaTiO<sub>3</sub>/Nb:STO film. No ferroelectric domains could be detected in the as-grown film, while such domains can be written, as shown in (b), with +6 V on the AFM tip in the outer square ( $4 \times 4 \mu\text{m}^2$ ) and -6 V in the inner square ( $2 \times 2 \mu\text{m}^2$ ). c,d) ARPES energy-momentum intensity maps at the Al(2 Å)/BaTiO<sub>3</sub> interface prepared in situ, using respectively 47 eV LV and 80 eV LH photons, the latter being close to  $\Gamma_{103}$ . e) Second energy-derivative of the ARPES map in (d). Vertical dashed red lines in c–e) are the Brillouin-zone edges. The red curve in (e) is a cosine fit to the heavy band. f,g) Spectral weight integrated over  $E_F \pm 30$  meV at the Al(2 Å)/BaTiO<sub>3</sub> interface using 80 eV LV and 47 eV LV photons, respectively. h) Capacitance–voltage curve on the Al(2 Å)/BaTiO<sub>3</sub> interface measured previously by ARPES, showing the butterfly shape characteristic of a ferroelectric hysteresis. A Pd circular pad and the Nb:STO substrate were used as top and bottom electrodes, respectively. Note that, due to the voltage drop through the thin alumina layer, the voltages  $V_c^+$  and  $V_c^-$  required to reverse the polarization are rather high. Thus, it was not possible to perform a polarization reversal in PFM mode.

Finally, Figure 3h shows a measurement of the capacitance–voltage curve on the same Al(2 Å)/BaTiO<sub>3</sub> interface that was measured by ARPES. The “butterfly” shape, with a difference of about 0.5 V between the two coercive voltages, demonstrates that the BTO film is still ferroelectric after deposition of the Al layer and ARPES measurements, thus keeping its functional behavior.

A 2DES at the surface of BaTiO<sub>3</sub> is in essence an intrinsic metal/ferroelectric interface. Polarization switching of the bulk material, for instance by strain, could allow a direct gating of the 2DES, while a sufficiently thick capping alumina layer protects it against re-oxidation at ambient conditions, and can be even used to draw metallic nanocircuits of intrinsic ferroelectric tunnel junctions. Thus this system provides a realistic platform for the realization of nonvolatile memories using ferroelectric resistive switching<sup>[29,30]</sup> or for ultrasensitive strain or pressure detectors.

In conclusion, the method we present here for realizing 2DESs in oxides has the advantages of simplicity and versatility—for instance, it can be readily implemented in many UHV setups, allowing future investigations of 2DESs in complex oxides with techniques that do not use synchrotron radiation, like tunneling or Raman spectroscopies. This method is

also pertinent for the study of transport phenomena in mesoscopic oxide devices. Indeed, STO has emerged as an exciting nanoelectronics device platform,<sup>[37]</sup> owing to the existence of superconductivity, spin–orbit interaction and magnetism, which are controllable with a gate voltage. Our work opens up new possibilities to explore these questions by making a wide range of transition–metal oxide 2DESs suitable for transport, including the surfaces, which are candidates for hosting topological electronic states.<sup>[23,24]</sup> Furthermore, the stability of the 2DES in ambient conditions can be achieved through a sufficiently thick layer of oxidized Al. This opens the possibility to integrate 2DESs in transition metal oxides into functional devices without the need of evolved deposition techniques.

## Experimental Section

The ARPES measurements were conducted at the CASSIOPEE beamline of Synchrotron SOLEIL (France). We used linearly polarized photons in the energy range 30–110 eV and a hemispherical electron analyzer with vertical slits. The angular and energy resolutions were 0.25° and 15 meV. The mean diameter of the incident photon beam was smaller than

100  $\mu\text{m}$ . The samples were cooled down to  $T = 8\text{ K}$  before measuring. Unless specified otherwise, all data were taken at that temperature. The results have been reproduced on more than 10 samples for  $\text{SrTiO}_3(001)$ , and on at least two samples for other surface orientations and for  $\text{TiO}_2$  anatase, and on three thin films of  $\text{BaTiO}_3/\text{SrTiO}_3(001)$ . All through this paper, reciprocal-space directions  $\langle hkl \rangle$  and planes  $(hkl)$  are defined in the conventional cell of each material (cubic for  $\text{SrTiO}_3$ , simple tetragonal for anatase and  $\text{BaTiO}_3$ ). The indices  $h$ ,  $k$ , and  $l$  of  $\mathbf{l}_{hkl}$  correspond to the reciprocal lattice vectors of the cubic unit cell ( $\text{SrTiO}_3$  and  $\text{BaTiO}_3$ ) or body-centered tetragonal unit cell (anatase).

Additional details on the sample and surface preparation, the Al deposition conditions, and the piezo-response force microscopy and capacitance–voltage measurements can be found in the Supporting Information.

## Supporting Information

Supporting Information is available from the Wiley Online Library or from the author.

## Acknowledgements

The authors thank illuminating discussions with M. Gabay and M.J. Rozenberg, and V. Pillard for help with the sample preparation. This work was supported by public grants from the French National Research Agency (ANR), project LACUNES No ANR-13-BS04-0006-01, and the “Laboratoire d'Excellence Physique Atomes Lumière Matière” (LabEx PALM project ELECTROX) overseen by the ANR as part of the “Investissements d'Avenir” program (reference: ANR-10-LABX-0039). T.C.R. acknowledges funding from the RTRA–Triangle de la Physique (project PEGASOS). A.F.S.-S. thanks support from the Institut Universitaire de France.

Received: October 12, 2015

Revised: November 19, 2015

Published online: January 11, 2016

- [1] A. Ohtomo, H. Y. Hwang, *Nature* **2004**, 427, 423.
- [2] S. Thiel, G. Hammerl, A. Schmehl, C. W. Schneider, J. Mannhart, *Science* **2006**, 313, 1942.
- [3] N. Reyren, S. Thiel, A. D. Caviglia, L. Fitting Kourkoutis, G. Hammerl, C. Richter, C. W. Schneider, T. Kopp, A.-S. Rüetschi, D. Jaccard, M. Gabay, D. A. Muller, J.-M. Triscone, J. Mannhart, *Science* **2007**, 317, 1196.
- [4] A. D. Caviglia, S. Gariglio, N. Reyren, D. Jaccard, T. Schneider, M. Gabay, S. Thiel, G. Hammerl, J. Mannhart, J.-M. Triscone, *Nature* **2008**, 456, 642.
- [5] A. Brinkman, M. Huijben, M. van Zalk, J. Huijben, U. Zeitler, J. C. Maan, W. G. van der Wiel, G. Rijnders, D. H. A. Blank, H. Hilgenkamp, *Nat. Mater.* **2007**, 6, 493.
- [6] L. Li, C. Richter, J. Mannhart, R. C. Ashoori, *Nat. Phys.* **2011**, 7, 762.
- [7] J. A. Bert, B. Kalisky, C. Bell, M. Kim, Y. Hikita, H. Y. Hwang, K. A. Moler, *Nat. Phys.* **2011**, 7, 767.
- [8] A.D. Caviglia, M. Gabay, S. Gariglio, N. Reyren, C. Cancellieri, J. M. Triscone, *Phys. Rev. Lett.* **2010**, 104, 126803.
- [9] M. Ben Shalom, A. Ron, A. Palevski, Y. Dagan, *Phys. Rev. Lett.* **2010**, 105, 206401.
- [10] A. F. Santander-Syro, A. F. Santander-Syro, F. Fortuna, C. Bareille, T. C. Rödel, G. Landolt, N. C. Plumb, J. H. Dil, M. Radovic, *Nat. Mater.* **2014**, 13, 1085.
- [11] H. Takagi, H. Y. Hwang, *Science* **2010**, 327, 1601.
- [12] J. Mannhart, D. G. Schlom, *Science* **2010**, 327, 1607.
- [13] H. Y. Hwang, Y. Iwasa, M. Kawasaki, B. Keimer, N. Nagaosa, Y. Tokura, *Nat. Mater.* **2012**, 11, 103.
- [14] N. Nakagawa, H. Y. Hwang, D. A. Muller, *Nat. Mater.* **2006**, 5, 204.
- [15] Y. Z. Chen, N. Pryds, J. E. Kleibecker, G. Koster, J. Sun, E. Stamate, B. Shen, G. Rijnders, S. Linderöth, *Nano Lett.* **2011**, 11, 3774.
- [16] S. W. Lee, Y. Liu, J. Heo, R. G. Gordon, *Nano Lett.* **2012**, 12, 4775.
- [17] J. Delahaye, T. Grenet, *J. Phys. D: Appl. Phys.* **2012**, 45, 315301.
- [18] E. Lesne, N. Reyren, D. Doennig, R. Mattana, H. Jaffrès, V. Cros, F. Petroff, F. Houeikani, P. Ohresser, R. Pentcheva, A. Barthélémy, M. Bibes, *Nat. Commun.* **2014**, 5, 4291.
- [19] A. F. Santander-Syro, O. Copie, T. Kondo, F. Fortuna, S. Pailhes, R. Weht, X. G. Qiu, F. Bertran, A. Nicolaou, A. Taleb-Ibrahimi, P. Le Fèvre, G. Herranz, M. Bibes, N. Reyren, Y. Apertet, P. Lecoeur, A. Barthélémy, M. J. Rozenberg, *Nature* **2011**, 469, 189.
- [20] W. Meevasana, P. D. C. King, R. H. He, S.-K. Mo, M. Hashimoto, A. Tamai, P. Songsiririthigul, F. Baumberger, Z.-X. Shen, *Nat. Mater.* **2011**, 10, 114.
- [21] A. F. Santander-Syro, C. Bareille, F. Fortuna, O. Copie, M. Gabay, F. Bertran, A. Taleb-Ibrahimi, P. Le Fèvre, G. Herranz, N. Reyren, M. Bibes, A. Barthélémy, P. Lecoeur, J. Guevara, M. J. Rozenberg, *Phys. Rev. B* **2012**, 86, 121107.
- [22] P. D. C. King, R. H. He, T. Eknapakul, P. Buaphet, S.-K. Mo, Y. Kaneko, S. Harashima, Y. Hikita, M. S. Bahrany, C. Bell, Z. Hussain, Y. Tokura, Z.-X. Shen, H. Y. Hwang, F. Baumberger, W. Meevasana, *Phys. Rev. Lett.* **2012**, 108, 117602.
- [23] C. Bareille, F. Fortuna, T. C. Rödel, F. Bertran, M. Gabay, O. H. Cubelos, A. Taleb-Ibrahimi, P. Le Fèvre, M. Bibes, A. Barthélémy, T. Maroutian, P. Lecoeur, M. J. Rozenberg, A. F. Santander-Syro, *Sci. Rep.* **2014**, 4, 1.
- [24] T. C. Rödel, C. Bareille, F. Fortuna, C. Baumier, F. Bertran, P. Le Fèvre, M. Gabay, O. Hijano Cubelos, M. J. Rozenberg, T. Maroutian, P. Lecoeur, A. F. Santander-Syro, *Phys. Rev. Appl.* **2014**, 1, 051002.
- [25] S. McKeown Walker, A. de la Torre, F. Y. Bruno, A. Tamai, T. K. Kim, M. Hoesch, M. Shi, M. S. Bahrany, F. Baumberger, *Phys. Rev. Lett.* **2014**, 113, 177601.
- [26] T. C. Rödel, F. Fortuna, F. Bertran, M. Gabay, M. J. Rozenberg, A. F. Santander-Syro, P. Le Fèvre, *Phys. Rev. B* **2015**, 92, 041106(R).
- [27] Q. Fu, T. Wagner, *Surf. Sci. Rep.* **2007**, 62, 431.
- [28] Q. Fu, T. Wagner, *J. Phys. Chem. B* **2005**, 3, 11697.
- [29] S.-I. Kim, D.-H. Kim, Y. Kim, S. Y. Moon, M.-G. Kang, J. K. Choi, H. W. Jang, S. K. Kim, J.-W. Choi, S.-J. Yoon, H. J. Chang, C.-Y. Kang, S. Lee, S.-H. Hong, J.-S. Kim, S.-H. Baek, *Adv. Mater.* **2013**, 25, 4612.
- [30] V. T. Tra, J.-W. Chen, P.-C. Huang, B.-C. Huang, Y. Cao, C.-H. Yeh, H.-J. Liu, E.A. Eliseev, A. N. Morozovska, J.-Y. Lin, Y.-C. Chen, M.-W. Chu, P.-W. Chiu, Y.-P. Chiu, L.-Q. Chen, C.-L. Wu, Y.-H. Chu, *Adv. Mater.* **2013**, 25, 3357.
- [31] N. C. Plumb, M. Salluzzo, E. Razzoli, M. Månsson, M. Falub, J. Krempasky, C. E. Matt, J. Chang, M. Schulte, J. Braun, H. Ebert, J. Minr, B. Delley, K.-J. Zhou, T. Schmitt, M. Shi, J. Mesot, L. Patthey, M. Radovic, *Phys. Rev. Lett.* **2014**, 113, 086801.
- [32] P. D. C. King, S. McKeown Walker, A. Tamai, A. de la Torre, T. Eknapakul, P. Buaphet, S.-K. Mo, W. Meevasana, M. S. Bahrany, F. Baumberger, *Nat. Commun.* **2014**, 5, 3414.
- [33] A. Schilling, T. B. Adams, R. M. Bowman, J. M. Gregg, G. Catalan, J. F. Scott, *Phys. Rev. B* **2006**, 74, 024115.
- [34] N. A. Pertsev, A. G. Zembilgotov, A. K. Tagantsev, *Phys. Rev. Lett.* **1998**, 80, 1988.
- [35] K. J. Choi, M. Biegalski, Y. L. Li, A. Sharan, J. Schubert, R. Uecker, P. Reiche, Y. B. Chen, X. Q. Pan, V. Gopalan, L.-Q. Chen, D. G. Schlom, C. B. Eom, K. J. Choi, *Science* **2004**, 306, 1005.
- [36] J. Chen, Y. Luo, X. Ou, G. Yuan, Y. Wang, Y. Yang, J. Yin, Z. Liu, *J. Appl. Phys.* **2013**, 113, 204105.
- [37] S. Goswami, E. Mulazimoglu, L. M. K. Vandersypen, A. D. Caviglia, *Nano Lett.* **2015**, 15, 2627.